SAND2013-2351C

Pitch Error and Shear Web Disbond Detection on Wind Turbine Blades for Offshore Structural Health and Prognostics Management

Noah J. Myrent[1], Joshua F. Kusnick[2], and Douglas E. Adams[3]
Purdue Center for Systems Integrity, Lafayette, IN, 47905

D. Todd Griffith[4]
Sandia National Laboratories, Albuquerque, NM, 87185

Operations and maintenance costs for offshore wind plants are estimated to be significantly higher than the current costs for onshore wind plants. One way to reduce these costs would be to implement a structural health and prognostic management (SHPM) system as part of a condition based maintenance paradigm with smart load management. To facilitate the development of such a system a multiscale modeling approach has been developed to identify how the underlying physics of the system are affected by the presence of damage and faults, and how these changes manifest themselves in the operational response of a full turbine. This methodology was used to investigate the effects of rotor imbalance and shear web disbond on a 5-MW offshore wind turbine in the present report. Based on simulations of the model, the operational measurements that demonstrated the highest sensitivity to the damage/faults were the blade tip accelerations and local pitching moments for both imbalance and shear web disbond. The integration of the health monitoring information provides the initial steps to reducing operations and maintenance costs for an offshore wind farm while increasing turbine availability and overall profit.

Nomenclature

G	=	mass imbalance grade
R_{eff}	=	effective span-wise location of the added mass
$S_k(f)$	=	turbulence model spectra
U_{per}	=	calculated change in blade mass
W	=	rotor mass

I. Introduction

As of June 2011, while nine offshore projects totaling over 2 GW of capacity were in various stages of the permitting and development process, no offshore wind energy projects had been installed in the United States[1]. Part of the reason for this lack of development is that operations and maintenance (O&M) costs are expected to be significantly higher for offshore wind turbines than onshore wind turbines. Recent projections of O&M costs have ranged between $11 and $66 U.S. dollars per megawatt-hour with the majority of estimates being between 2 to 5 times the cost of onshore O&M[2]. These higher O&M costs represent a larger overall proportion of the cost of energy than for onshore turbines even when the large initial investment required for the installation of offshore turbines is included[3]. One of the reasons that O&M costs are likely to be higher offshore is that the offshore environment will bring with it increased loading which is relatively uncharacterized due to the lack of

[1] Research Engineer, Purdue Center for Systems Integrity, nmyrent@purdue.edu, AIAA Member
[2] Graduate Student, Department of Mechanical Engineering, josh.kusnick@gmail.com
[3] Kenninger Professor of Renewable Energy and Power Systems, Department Mechanical Engineering, deadams@purdue.edu, AIAA Associate Fellow or Senior Member.
[4] Offshore Wind Technical Lead, Wind and Water Power Technologies, dgriffi@sandia.gov, AIAA Senior Member.

existing offshore installations. Offshore turbines will also have to be built to withstand the environmental harshness of the offshore environment. Lastly, access to the turbines will be difficult, costly, and occasionally not possible due to high sea states[2,6].

One potential way in which these O&M costs could be addressed is through the use of a structural health and prognostics management (SHPM) system as part of a condition based maintenance (CBM) paradigm[4-10]. By continuously monitoring the health, or condition, of structural components in each wind turbine, required maintenance actions can be scheduled ahead of time and performed when they are needed rather than on a preset schedule or only after failure has already occurred. The benefits of a CBM strategy are expected to include less regular maintenance, the avoidance or reduction of unscheduled maintenance and improved supply chain management[6-9].

In an effort to map out the SHPM problem with application to wind turbine rotor blades and also provide an example case study, an initial roadmap was developed by Sandia National Laboratories for a combining structural health monitoring and prognostics management assets into a SHPM system as documented in Reference 12. The key element established in this initial roadmap, the so-called multi-scale damage modeling and simulation methodology, addresses both how damage is modeled at multiple resolutions of the model and also the resulting manifestation (or effects) of damage in both the global operating dynamic response and localized effects related to remaining life. The intent of this approach is to combine structural health monitoring and prognostic management so as to bridge the gap between being able to detect and characterize the presence of damage and then being able to make operations and maintenance decisions.

Furthermore, because wind turbines are active systems, monitoring the health of wind turbine components will allow for smart turbine load management to optimize the profit of the entire wind plant. For example, if a turbine blade becomes damaged and that damage is detected at an early stage by the SHPM system, the turbine could be derated so that small less costly repairs could be performed on the turbine. While this action would reduce the amount of power generated by the turbine in the short-term, it may allow for less extensive maintenance actions to be performed, permit additional energy capture while maintenance is being planned, extend the overall life of the turbine, and allow for multiple turbines to be serviced during the same visit to maximize the overall profit of the wind power plant.

II. Five Megawatt Offshore Turbine Model

As part of an ongoing structural health and prognostics management project for offshore wind turbines, the simulations in this report were performed using a representative utility-scale wind turbine model. The model, known as the NREL offshore 5-MW baseline wind turbine model, was developed by NREL to support studies aimed at assessing offshore wind technology[11]. It is a three-bladed, upwind, variable-speed, variable blade-pitch-to-feather-controlled turbine and was created using available design information from documents published by wind turbine manufacturers, with a focus on the REpower 5-MW turbine. Basic specifications of the model configuration are listed in **Error! Reference source not found.**e 1.

Table 1. Gross Properties of the NREL 5-MW Baseline Wind Turbine [11]

Property	Value
Rating	5MW
Rotor Orientation, Configuration	Upwind, 3 blades
Control	Variable Speed, Collective Pitch
Drivetrain	High Speed, Multiple-Stage Gearbox
Rotor, Hub Diameter	126 m, 3 m
Hub Height	90 m
Cut-in, Rated, Cut-out Wind Speed	3 m/s, 11.4 m/s, 25 m/s
Cut-in, Rated Rotor Speed	6.9 rpm, 12.1 rpm
Rated Tip Speed	80 m/s
Overhang, Shaft Tilt, Precone	5m, 5°, 2.5°
Rotor Mass, Nacelle Mass, Tower Mass	110,000 kg; 240,000 kg; 347,460 kg
Water Depth	20 m
Wave Model	JONSWAP/Pierson-Moskowitz Spectrum
Significant Wave Height	6 m
Platform	Fixed-Bottom Monopile

Two thirds of the blade span utilizes the TU-Delft family of airfoils, while the final one-third of the blade span utilizes the NACA 64-series airfoils. Intermediate airfoil shapes were developed that preserve the blending of camber lines as well as a smooth blade thickness profile. Figure 1 shows the finite element model of the blade in ANSYS with the colored sections representing different composite materials. This high degree-of-freedom model was translated into a model consisting of several beam elements using Sandia's Blade Property Extraction tool (BPE)[6]. BPE works by applying loads in each of the six degrees of freedom at the tip of the blade model in ANSYS, then processing the resulting displacements at selected nodes along the blade to generate the 6x6 Timoshenko stiffness matrices for the beam discretization. This reduced degree-of-freedom model is subsequently used to define the blade properties in FAST.

Figure 1. ANSYS finite element mesh for the 5-MW blade model

FAST uses six coordinate systems for input and output parameters[13]. Note that the FAST User's Guide coordinate system images use a downwind turbine configuration; however, the same coordinate systems apply in the case of the upwind turbine being referred to in this work, but the orientation of the x axis changes so that in either configuration it is pointing in the nominally downwind direction. The rotor shaft coordinate system is shown in Figure 2a. This coordinate system does not rotate with the rotor, but it translates and rotates with the tower and yaws with the nacelle. In addition to output variables related to the low speed shaft, the nacelle inertial measurements also use this coordinate system. Some shaft outputs, such as shear force in the low speed shaft, are measured in both a non-rotating coordinate system and a rotating coordinate system; these are differentiated by using an "s" or "a" subscript, respectively. The tower base coordinate system shown in Figure 2b is fixed in the support platform, thus rotating and translating with the platform. The tower-top/base-plate coordinate system shown in Figure 2c is fixed to the top of the tower. It translates and rotates with the motion of the platform and tower top, but it does not yaw with the nacelle.

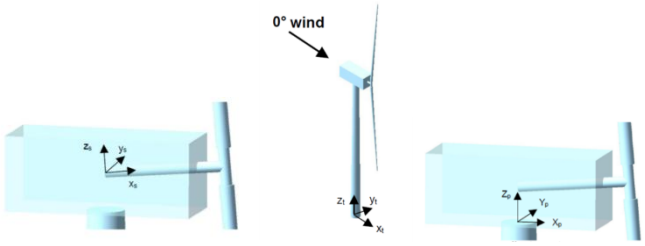

(a) **(b)** **(c)**

Figure2. (a) Shaft Coordinate System[13]; (b) Tower Base Coordinate System[13]; (c) Tower-Top/Base-Plate Coordinate System[13]

III. Rotor Mass/Aerodynamic Imbalance Sensitivity Study

Computer simulations were carried out using the 5-MW turbine model described in Section II. Modeling was performed using NREL's Fatigue, Aerodynamics, Structures and Turbulence (FAST) code, which is a comprehensive aeroelastic simulator for two and three-bladed horizontal axis wind turbines (HAWTs). The code provides the means to manipulate a variety of input parameters, including turbine control settings, environmental conditions, blade and tower models, drivetrain and generator parameters, and many others. There are also hundreds of possible outputs, including blade inertial measurements and generator power.

FAST uses AeroDyn to calculate the aerodynamics of HAWTs. AeroDyn is an aeroelastic simulation code which uses several subroutines for wind turbine applications, including the blade element momentum theory, the generalized dynamic-wake theory, the semi-empirical Beddoes-Leishman dynamic stall model, and a tower shadow model. The FAST model combines a modal and multibody dynamics formulation, and performs a time-marching

analysis of the nonlinear equations of motion. For a more detailed description of the working principles of the code, see the FAST User's Guide[13].

Imbalance of the rotor can occur for a number of reasons, although the imbalance can generally be divided into two categories: mass imbalance or an aerodynamic imbalance. Pitch error is a common problem that fits into a more general class of turbine faults referred to as aerodynamic asymmetries. This means that the individual blades are not generating the same thrust and tangential forces when subjected to the same wind profile. Other reasons this can occur are blade profile differences as a result of manufacturing tolerances, blade surface roughness changes, and degradation or damage to a blade, such as tip delamination, erosion, or deformation of the structure. Since the effects of aerodynamic asymmetries are closely related to rotor mass imbalances and information to-date indicates that 20% of utility-scale wind turbines have a mass or aerodynamic imbalance[14], both types of imbalances were simulated in this work. Mass imbalances result from inhomogeneous mass distributions in the blades caused by manufacturing, water inclusions, icing, and loose material from manufacturing moving inside the blade towards the tip during rotation[15]. Existing or proposed imbalance detection methods in wind turbines use inertial measurements in the nacelle. However, there are difficulties using this method which are illustrated using a simplified rotor dynamics model in the next section. Therefore, several methods of detection were evaluated in order to compare the use of blade and non-blade measurements, and a detection algorithm is proposed and summarized in this paper.

A. Imbalance Simulation Methods

To eliminate possibilities of some confounding variables such as yaw error and to study the effects of aerodynamic asymmetries and mass imbalances alone, simulations were carried out in a unidirectional, constant-speed, vertically sheared wind environment, rather than using the random and turbulent wind input conditions that are also available as inputs in FAST. The wind direction was oriented at 0°, directly perpendicular to the rotor plane, and the yaw degree of freedom was turned off in the FAST input file. The wind speed was set to 11 m/s, with a 1/7 power law vertical shear profile. Setting the wind speed to just below the rated speed of 11.4 m/s ensured that in the case of pitch error of a single blade, the two actively-pitching blades would always pitch to zero degrees to maximize the power output of the turbine, thus keeping those variables constant. The sample time spacing was set to 0.01 seconds, corresponding to a sample rate of 100 Hz. Because the per-revolution harmonics were mainly of interest and the maximum rotor speed was 12.1 rpm, or 0.2 Hz, this sample rate was sufficient. Simulations were conducted in three phases: (1) aerodynamic asymmetries, (2) mass imbalances, and (3) simultaneous aerodynamic and mass imbalances. Two hundred output variables were recorded from the simulations, including generator power, low speed shaft torque, tri-axial blade accelerations along the span, nacelle accelerations, and many others for use in the sensitivity of damage/fault studies.

In this phase of simulation, a rotor mass imbalance was applied by increasing the mass density of blade three at a particular blade span-wise section in the FAST blade input file. The magnitudes of the mass imbalances chosen were based on two references. The first is the acceptable residual imbalance method employed by Pruftechnik Condition Monitoring GmbH, a German company which performs field-balancing of wind turbine rotors[14]. This company applies a fairly standard field balancing procedure: initial vibration measurements are taken from within the nacelle, a trial mass is added to the rotor and its effects are measured, and the balancing software then determines suggested balancing weights and locations. A detailed explanation of the general rotor balancing procedure and calculations can be found in Bruel & Kjaer's application notes[16]. Pruftechnik quantifies the permissible residual imbalance based on the standard DIN ISO1940-1: Mechanical Vibration – Balance Quality Requirements for Rotors in a Constant (Rigid) State – Part 1: Specification and Verification of Balance Tolerances. This standard provides permissible residual imbalance levels in the rotor, with different quality grades, G, depending on the application. The imbalance magnitude is found using the rotor's operational speed, rotor weight, and the balancing radius, which is the span location of the mass imbalance. Plots in the standard provide the permissible imbalance in gram-mm/kg which are based on the rotor speed and G grade. A second source for determining mass imbalance testing levels was Moog Incorporated's fiber-optic based rotor monitoring system, which claims imbalance detection down to 0.5% of the total blade mass of all three blades[17]. For consistency and ease of comparison, it will be assumed that this imbalance is acting at the mass center of a single blade, and it will be translated to an ISO1940-1 G quality grade.

The FAST blade input file for the blade model contains 23 section locations for specifying section properties. However, for computational purposes, the 23 locations are interpolated down to 17 nodes as specified in the AeroDyn input file for application of the aerodynamic forces in FAST. Therefore, the following procedure was followed to ensure that mass imbalance specified in the 23-section FAST blade input file would result in the intended G grade after interpolation:

1.) A MATLAB script was written to apply the same piecewise linear interpolation found in FAST's FORTRAN source code. The accuracy of the code was verified by adjusting the FAST input blade properties and comparing the output of the script to the interpolated blade properties that are output from FAST.

2.) The mass density of one or more of the 23 blade sections was altered and the interpolated blade section properties were then computed by the script.

3.) The script determined which interpolated blade sections incurred mass density changes compared to the interpolated properties of the unaltered blade.

4.) The effective span-wise location of the added mass was computed using a moment balance as follows in equation (1):

$$R_{eff} = \frac{\sum_{i=1}^{N} (dm)_i \cdot (dr)_i \cdot r_i}{\sum_{i=1}^{N} (dm)_i \cdot (dr)_i}, \tag{1}$$

where R_{eff} is the effective span-wise location of the added mass, N is the number of blade sections, $(dm)_i$ is the change in mass density of blade section *i* in kg/meter, $(dr)_i$ is the length of the i^{th} blade section in meters, and r_i is the radial location of the blade section in meters.

5.) The rotor mass, W, was computed using the newly interpolated blade mass properties in addition to the hub mass. The rotational speed N was found by running the simulations, which was 11.8 rpm regardless of the mass imbalance applied in these tests. The imbalance being applied was equal to the calculated change in mass in step 4, which was input as U_{per}. Finally, the mass imbalance was applied at R_{eff}, and the equation was formulated and solved for G:

$$G = \frac{U_{per} \cdot N}{9549 \cdot W} \cdot 10^6 R_{eff}. \tag{2}$$

It is possible that aerodynamic asymmetry and mass imbalance are present simultaneously in a wind turbine rotor. This presents the greatest challenge for a rotor imbalance condition monitoring system, that is, distinguishing between mass and aerodynamic imbalance. Two basic cases are considered: (1) the mass imbalance was located on blade three, while the pitch error occurred for blade two, and (2) the mass imbalance and pitch error both occurred on blade three. Only a small number of test cases were run with the goal of determining which detection algorithms were successful at detecting the simultaneous imbalances, ignoring the sensitivity of the algorithms to simultaneous imbalances.

B. Analysis of Imbalance without Blade Sensors

In order to compare the effectiveness of imbalance detection methods with and without blade sensors, algorithms were first generated for determining imbalance using only the outputs from FAST that would not require blade-mounted sensors. From the 200 variables which were generated at outputs from the FAST simulation, those which displayed a significant percentage change in their RMS value or frequency response magnitude at multiples of the operating speed for a given a mass imbalance or pitch error were identified as key measurement channels. Imbalance tends to excite the 1p frequency in the order domain. It has also been shown that the 2p and 3p harmonics can be influenced by aerodynamic imbalances, especially in the presence of wind shear[18], thus the 1p, 2p, and 3p frequencies were reviewed for changes in magnitude from the baseline tests.

The rotor azimuth position output from FAST was used as the reference signal for time synchronous averaging. To perform rotational resampling, the azimuth signal was converted to radians, was unwrapped and then the measurement signal was interpolated so that each revolution contained the same number of data samples with each sample corresponding to the same azimuth position of the rotor's rotation. Finally, blocks of three revolutions were averaged together; more than one revolution was used in the block size to increase the length of the block's time history, thereby increasing the frequency resolution of the DFT of the averaged signal. The imbalance detection algorithms for non-blade sensors all functioned similarly through the detection of changes from baseline measurements either in the RMS response or in the power spectral density magnitude at 1p, 2p, or 3p.

The generator power output displayed unique and readily identifiable changes due to pitch error when the wind speed is below the rated speed for the turbine, as it was for these simulations. **Error! Reference source not found.** 3a shows the expected result that as the pitch error of blade three increases, the mean power output of the turbine decreases significantly due to the reduced aerodynamic efficiency of the incorrectly pitched blade. Moreover, the zoomed-in view of one revolution of the TSA power signal in **Error! Reference source not found.** 3b shows that the power output shifts from having predominantly 3p oscillations for zero pitch error to a progressively larger 1p fluctuation with increasing pitch error. The magnitude of the 1p component most likely decreases as pitch error moves above 7.5° because the reduced rotor speed has consequently reduced the loading magnitude. The 3p oscillation for zero pitch error is a common occurrence due to the increased wind speeds caused by vertical wind shear and seen by the upright, 0° azimuth positioned blade. This occurs three times per revolution, once as each blade passes the 0° position, resulting in larger aerodynamic forces on that blade and thus a 3p oscillation in rotor torque. It should also be noted that the rotor torque signal displayed very similar characteristics to the generator power output. Because the generator power can be subject to electrical faults as well, analyzing rotor torque measured at the low speed shaft may be a better indicator of mechanical behavior in the field.

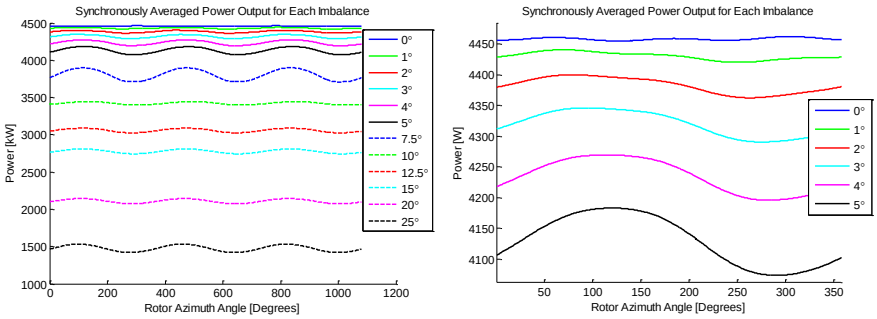

(a) **(b)**

Figure 2. (a) Three revolution time synchronously averaged power output for each pitch error test;(b) Single revolution zoomed-in single revolution TSA power output for pitch errors of 0° to 5°

Nacelle inertial measurements are often recommended in wind turbine condition monitoring literature for detecting rotor imbalance. For all subsequent discussion, axial nacelle acceleration will refer to acceleration in the x_s direction. Transverse nacelle motion is in the side-to-side direction, which is the y_s axis. The 1p component of the axial acceleration of the nacelle should be indicative of an aerodynamic imbalance. Similarly, the moments about the transverse and vertical axes, y_s and z_s shown in **Error! Reference source not found.** 2a, respectively, should also be affected in their 1p response by aerodynamic imbalance. However, instead of plotting the moment outputs from FAST, the nacelle angular acceleration outputs were used and the magnitude of the 1p PS of each of those measurements, as well as the nacelle axial and transverse accelerations, are shown in **Error! Reference source not found.** 4.

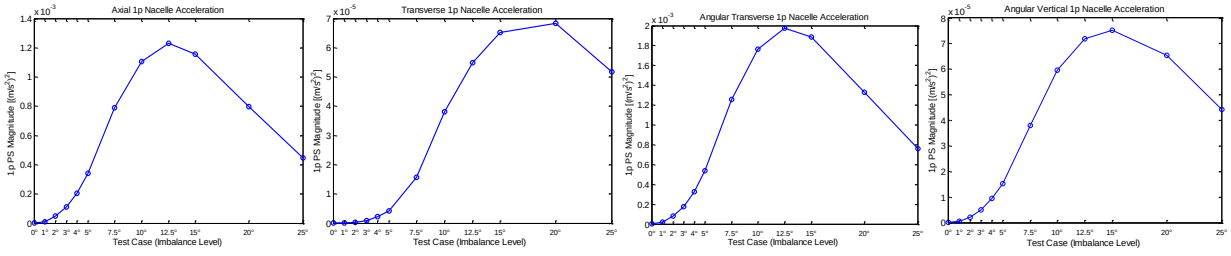

Figure 4. Nacelle axial and transverse accelerations and angular accelerations about the transverse and vertical axes vs. pitch error

The 1p PS magnitude follows a similar trend in both the axial nacelle acceleration and the angular nacelle acceleration about the transverse axis. For 12.5° pitch error and greater, the 1p magnitude begins to fall, which is again likely due to decreased loading magnitude from the reduction in rotor speed. Interestingly, the transverse

nacelle acceleration shows a similar trend and does not begin to fall off until 25° pitch error. However, these oscillations are two orders of magnitude lower than the axial acceleration, and the 1p magnitude changes less rapidly in the 0°-5° range, making this a less sensitive measurement channel for low pitch error. Finally, the angular acceleration about the vertical nacelle axis displays a similar trend to the transverse angular acceleration, but is two orders of magnitude lower.

In the case of mass imbalance, the mean power remain unchanged but the magnitude of the 1p PS of the inertial measurements was three or more orders of magnitude lower than the acceleration generated by the pitch errors. The trend of increasing 1p PS is very similar in all four inertial measurements in **Error! Reference source not found.** 5. The transverse nacelle acceleration is greater than the acceleration in the axial direction in agreement with the literature, but all four accelerations are so small that they would be very difficult to measure.

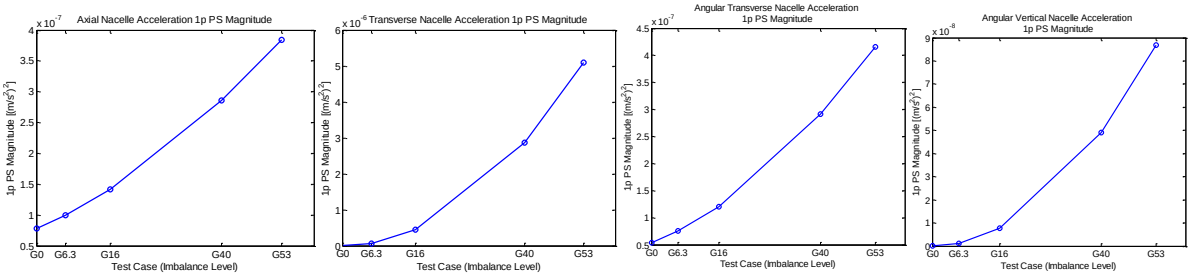

Figure 5. Nacelle axial and transverse accelerations and angular accelerations about the transverse and vertical axes for mass imbalance

Simulations were also performed for a simultaneous mass and aerodynamic imbalance applied to the rotor. Included are tests with mass and aerodynamic imbalances applied to the same blade, blade three, as well as tests in which blade three contained the increased mass and blade two exhibited pitch error. The syntax for the plot legends and axis labels referring to the different test cases is as shown in **Error! Reference source not found.** 6. If no mass or aerodynamic imbalance was applied in the test, the "B" corresponding to that imbalance will be followed by a zero. Moderate mass and aerodynamic imbalance levels were chosen for these simulations: G16 and G40, and 3° and 5° pitch errors. To aid in quantifying the difference between the simultaneous imbalance cases, each mass imbalance was also applied with no simultaneous pitch error for comparison. The same three non-blade measurements, generator power output, nacelle inertial sensors, and low speed shaft bending moments are once again examined.

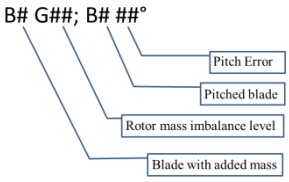

Figure 6. Simultaneous mass and aerodynamic imbalance test designation syntax

The generator power output for these tests coincides with what is expected from the results of individual mass and aerodynamic imbalance in the previous sections. **Error! Reference source not found.**s 7 and 8 show that there are three distinct groups of test conditions with the same mean power output: those tests with the same pitch error, regardless of the mass imbalance or which blade was pitched, generate the same mean power. The mean power levels were 4458 kW, 4319 kW, and 4130 kW for pitch errors of 0°, 3°, and 5°, respectively.

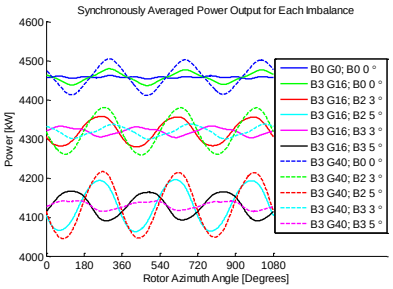

Figure 7. Three-revolution TSA power output for each simultaneous imbalance test

Error! Reference source not found. 8a confirms that the 1p PS magnitude of the power signal is dependent on both the mass and aerodynamic imbalance, as was demonstrated in the previous sections. Interestingly, it also reveals that the 1p response is greater if the mass addition and aerodynamic imbalance are on different blades, as can be seen by comparing the B3G16, B2 3° case to the B3G16 B3 3° case, for instance. A more intuitive response is found when looking at the 2p frequency in the order domain, as shown in **Error! Reference source not found.** 8b. It shows that the 2p PS magnitude is largely dependent on the pitch error; however, when the added mass is on a different blade than the one undergoing pitch error, the 2p response is higher, again as in the B3G16, B2 3° and B3G16, B3 3° cases, where the magnitude changes by about 3.5%. Furthermore, the 2p response also increases for increasing mass imbalance. Although the changes look fairly small when compared to the changes brought about by pitch error, the response increases by about 3% from B3G16, B2 5° to B3G40 B2 5°, for example. So, it may be possible to determine if there are simultaneous mass and aerodynamic imbalances from the generator power. However, it would likely require a fairly accurate simulation model to determine the response PS thresholds and this method is still ineffective in determining which blades are responsible for the mass or aerodynamic imbalance.

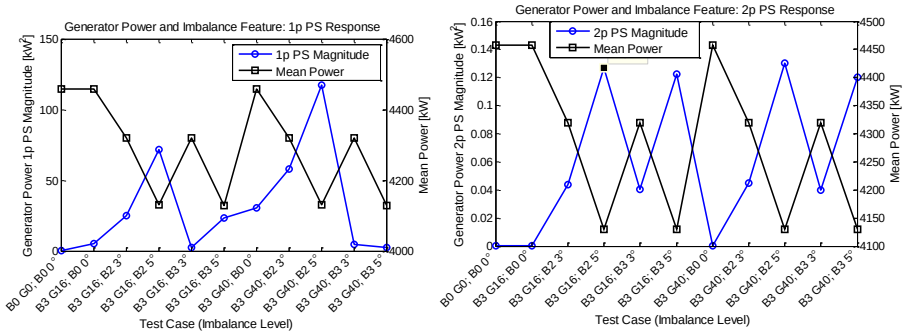

(a) **(b)**

Figure 8. (a) Mean generator power and 1p PS magnitude; (b) Mean generator power and 2p PS response

We again consider the 1p nacelle inertial responses. The axial nacelle acceleration and the two angular accelerations follow a very similar trend to the 2p generator power PS magnitude, as shown in **Error! Reference source not found.** 9. The angular accelerations look nearly identical to the axial acceleration and have therefore been omitted. Pitch error accounted for the largest percentage differences in the response. When pitch and mass imbalances were applied to different blades, the response was higher than when the same imbalance levels were applied to the same blade. The transverse nacelle acceleration response is less clear. In theory, the transverse response should be more sensitive to mass imbalance than pitch error, but it is clearly affected largely by pitch error[19]. The response seems to follow an expected trend from the first test case up to B3 G16, B3 5°. After that point, it would seem that the trend should restart, but with a higher initial value due to the larger G40 mass imbalance. The B3 G40, B0 0° response is indeed higher than B3 G16, B0 0°, but the response takes an unexpected dip at B3 G40, B2 3° and 5°. The likely cause is that the B3G40 and B2 3° and 5° errors cause similar transverse nacelle accelerations, as indicated in **Error! Reference source not found.** 5, but these responses are out of phase when the imbalances are applied to different blades. Therefore, phase is another important consideration when examining non-blade measurements for simultaneous imbalances acting on different blades.

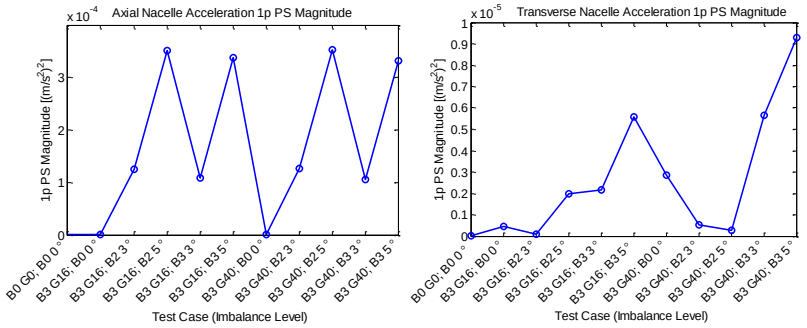

Figure 9. Nacelle axial and transverse accelerations for simultaneous imbalance

C. Analysis of Imbalance with Blade Sensors

In Section II-C, it was illustrated that some non-blade measurements provide good insight into detecting the presence of a mass or aerodynamic imbalance in the rotor and assessing its level of severity, but they lacked the ability to determine which blade(s) is the culprit (i.e. location), and in general provided confounding results when mass and aerodynamic asymmetries were simultaneously present. The next sections will examine outputs from the FAST simulations that would depend on blade-mounted sensors in an operating turbine.

The mean flap, RMS flap and edge degree-of-freedom blade accelerations are shown in the left two plots of **Error! Reference source not found.** 35. The mean flap response of the pitched blade three decreases significantly with increasing pitch error. As with some of the non-blade responses, the other two blade flap responses also begin to decrease around 7.5° as a result of reduced forcing from the slowed rotor. For that reason, it is helpful to examine the blade-to-blade differences in the response, shown in the right two plots in **Error! Reference source not found.** 10. The plot legend indicates which two blade responses have been subtracted from one another; the first blade listed has been subtracted from the second one. For instance, the blue line, Blades 1 & 2, shows the result of subtracting blade two's response from blade one's response. If the blade responses were all the same or very close, then no pitch error is present. When two blade-to-blade differences change, it can indicate the problematic blade. **Error! Reference source not found.** 11 illustrates which blade may be problematic (the terminal point of the arrows) based on which pair of blade-to-blade differences is different than the third (the starting point of the arrows). This method is also beneficial because it can eliminate the need for baseline data, but thresholds would still need to be set to determine what level of response difference indicates an error. Note that in the blade-to-blade differences in **Error! Reference source not found.** 10, blades 1 and 3 and blades 2 and 3 are grouped together, correctly indicating that blade 3 is the pitched blade. The absolute value of the difference was not plotted in **Error! Reference source not found.** 35 because in some cases, the sign of the difference can be an indicator of the pitch error. For instance, the lead-lag RMS tip acceleration is lower for the pitched blade until 7.5° pitch error but at 7.5° and above the pitch error is higher. Therefore the sign of the difference helps distinguish between a 5° and 7.5° pitch error, which are close in magnitude but opposite in sign. Finally, the response of blade 1 and 2 is slightly different; this is thought to be caused by blade 2 passing through the wake of the incorrectly pitched blade 3 as it rotates.

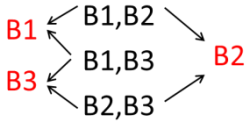

Figure 10. Diagram to determine faulty blade using blade-to-blade differences

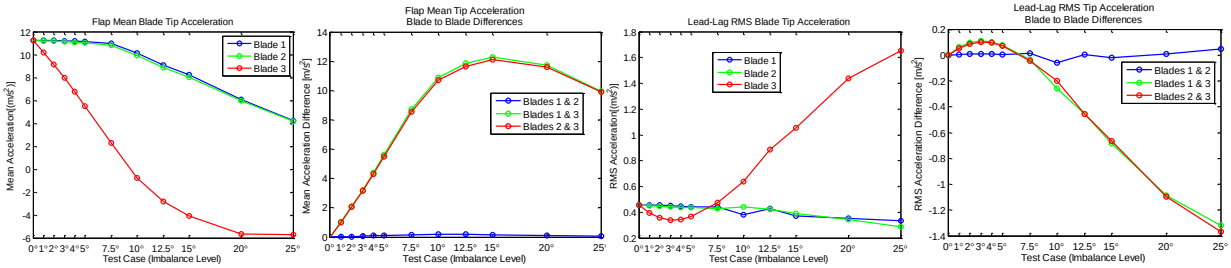

Figure 11. Flap and edgewise blade tip accelerations and blade-to-blade differences for pitch error

Note that the flap response is much more sensitive to low pitch error, 5° or less, than the nacelle axial response shown previously in **Error! Reference source not found.** 4. This makes the blade response a valuable tool in diagnosing aerodynamic imbalances. Lastly, **Error! Reference source not found.** 12 demonstrates that the 1p PS magnitude of the edgewise blade tip acceleration is a fairly good indicator of pitch errors above about 3°. Again, the differences in the response magnitude of blade 1 and 2 are thought to be caused by blade 2 passing through the wake of the pitched blade 3 during rotation.

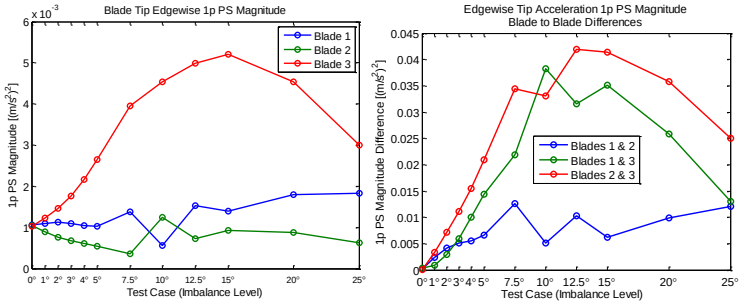

Figure 12. Blade tip edgewise 1p PS magnitude and blade to blade differences

The moment of the blade about its pitch axis at the blade root is another good indicator of pitch error, as shown in **Error! Reference source not found.** 13. It should be noted that the root pitching moment was also the most sensitive parameter to a trailing edge disbond, as shown in last year's work. This moment can be measured using strain gages located at the root of each blade. Again it is seen that the 1p PS magnitude tends to fall off due to reduced forcing from the slowed rotor for pitch errors greater than 10°, but the mean pitching moment of the pitched blade continues to decrease relative to the other two. Note that the plot in the lower right of **Error! Reference source not found.** 13 displays the absolute value of the mean difference.

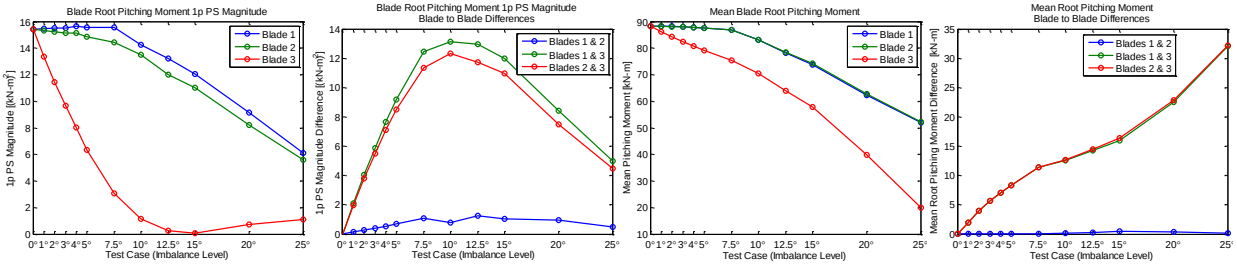

Figure 13. Blade root pitching moment 1p PS magnitude, RMS, and blade-to-blade differences

The mean (or RMS) flap and edge blade tip acceleration responses were indicative of pitch error and could identify which blade was pitched incorrectly. This remained true even when mass imbalances were present, as shown in **Error! Reference source not found.** 14. Note that the 1p lead-lag response was still a good indicator of pitch error, as was the span acceleration response, but both were left out for the sake of brevity. In experimental testing, the span and lead-lag degrees of freedom tend to exhibit less measurement noise and variance and therefore may be more beneficial than the flap degree of freedom measurement for use in statistics-based condition monitoring systems.

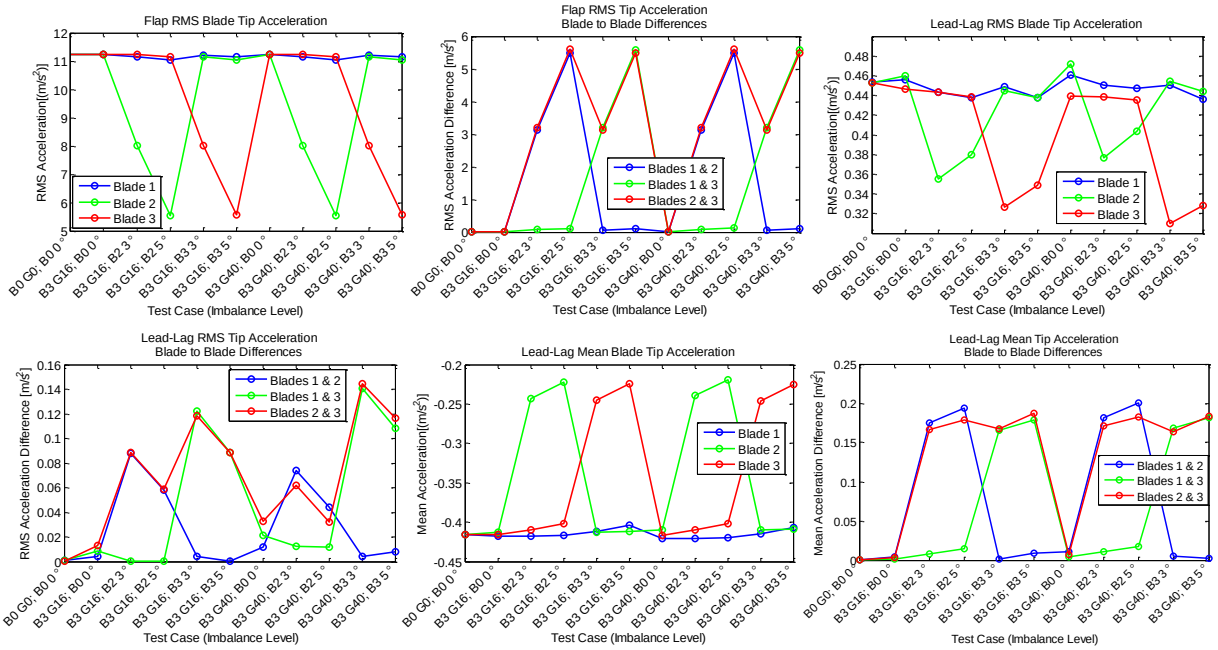

Figure 14. Span and edgewise blade tip accelerations and blade-to-blade differences for simultaneous mass imbalance and pitch error

The RMS and 1p PS magnitude of the blade root pitching moments decreased very consistently for the pitched blade, as seen in **Error! Reference source not found.** 15. For instance, the 1p PS magnitude of blade two's pitching moment when it had a pitch error of 3° is nearly the same as the pitching moment of blade three when it had the same pitch error. Note that the mass imbalances were evenly distributed throughout the affected blade section(s). If the mass imbalance were concentrated on the leading or trailing edge of the blade, it is feasible that this too may increase the pitching moment of the blade.

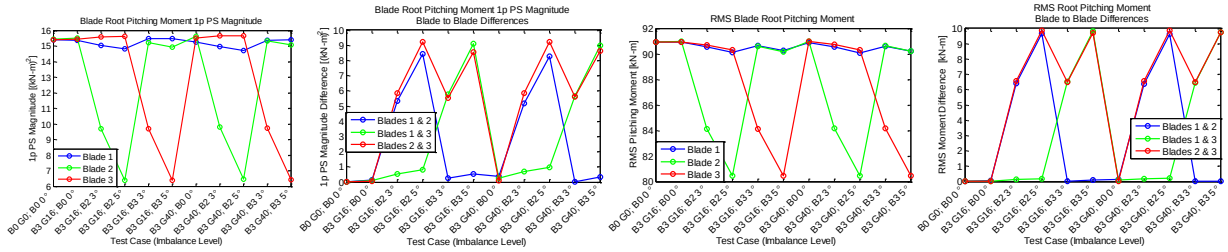

Figure 15. RMS, 1p PS, and blade-to-blade differences of blade root pitching moments for simultaneous mass imbalance and pitch error

D. Summary of Imbalance Detection Strategy

The results of these analyses can be synthesized into a flow chart, as shown in **Error! Reference source not found.** 16, for detection of rotor imbalances using a combination of sensors and analysis methods. This strategy utilizes both blade and non-blade sensor measurements. None of the methods evaluated thus far were successfully able to identify the blade having a mass imbalance; however, based on the above sensitivity studies of various imbalance conditions several methods have been developed to etect the presence of pitch error, its severity, as well as to identify which blade the pitch error is present. Therefore, and in summary, the strategy is as follows:

(1) Detect if an imbalance exists in the rotor

(2) Determine if the imbalance is strictly a mass imbalance, or whether it is a pitch or pitch and mass combination (it cannot yet be distinguished if there is just a pitch error or a simultaneous pitch error and mass imbalance at this stage)
(3) If the error is due to pitch or pitch and mass, determine which blade is pitched incorrectly and by how much. Correct this blade pitch through the blade control algorithm.
(4) Iterate until pitch error has been eliminated. If a mass imbalance is still present, it will then be identified, including which blade is the source of the imbalance.

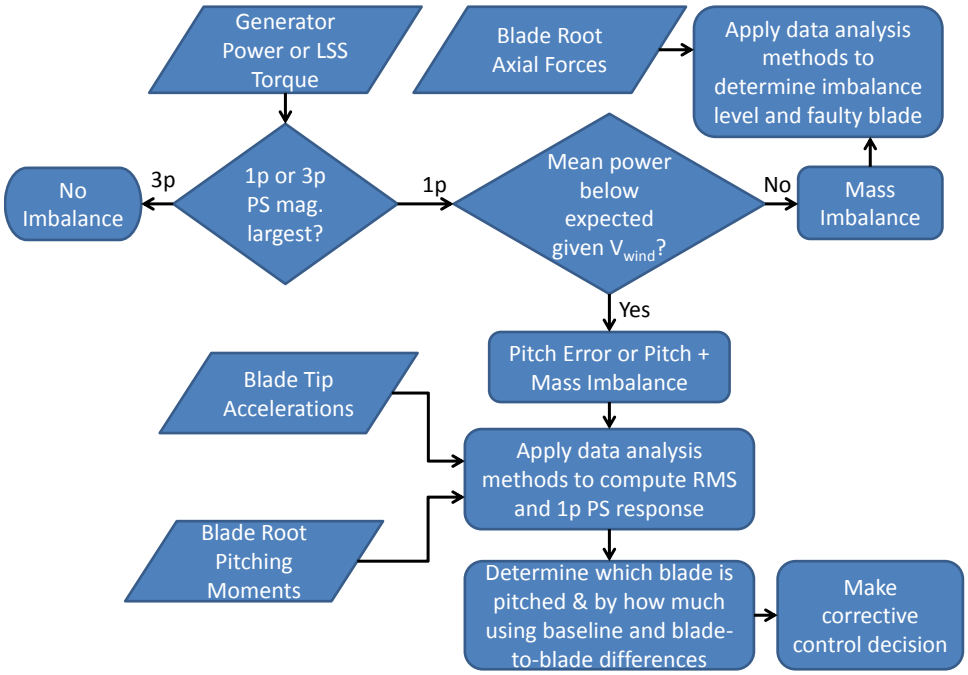

Figure 16. Pitch error and mass imbalance detection flow chart.

IV. Shear Web Disbond Sensitivity Study

The developed multiscale modeling methodology was utilized to investigate the sensitivity of a wide range of potential operational measurements to the presence of a shear web (SW) disbond. This representative form of damage was chosen because it is a damage mechanism that is routinely seen in the field. For this initial investigation all of the disbonds were assumed to have initiated at max chord of the blade (14.35 meters down the blade in the span-wise direction) and propagated outwards toward the tip of the blade. This section includes a variety of different sensitivity analyses that were conducted at various stages throughout the modeling and simulation processes.

A. Shear Web Disbond Damage Modeling Methodology and Simulation Methods

To model the presence of a shear web disbond on a wind turbine blade, the NuMAD blade model was modified so that each of the shear web nodes were split into two different nodes. This effectively split the blade model at the shear web in a similar way to how the blade is physically constructed through bonding the high pressure clam shell to the shear webs. To simulate a healthy bond across the blade, the top and bottom shear web nodes were connected using constraint equations in all six degrees of freedom. In the area of the blade in which the shear web disbond existed, the constraints were removed so that there was no connection between the top of the blade and the shear web. A similar approach was done by Griffith, et al. (2011) to simulate a trailing edge disbond on the same blade model[12]. While this modeling disbond methodology is effective in modeling a disbond in which the blade and shear web do not come into contact, it fails to take into account the possible interaction of the top and bottom surfaces of the disbond. For large cracks in which interaction between the top of the blade and the shear web may have a

significant influence, the relative decrease in stiffness due to the disbond is likely over-estimated because the added stiffness due to the disbond face interaction was not taken into account. Modeling the interaction between the two surfaces could be achieved using nonlinear surface contact constraints between the top of the blade and the shear web but this was not accomplished during this initial investigation and remains as future work.

FAST simulations were performed for several wind profiles and turbine blade conditions. Among the wind profiles used were constant wind speed and direction, IEC Kaimal Model with A turbulence, IEC Kaimal Model with B turbulence, and the NREL NWTC wind model with a KHTEST intense disturbance. For the constant wind profile, the wind speed was set to 11.4 m/s, with a 1/7 power law vertical shear profile. The IEC Kaimal model is defined in IEC 61400-1 2nd ed. and assumes neutral atmospheric stability[20]. A mean wind speed of 13 m/s was used. The spectra for the three wind components, K = u, v, w, are given by

$$S_K(f) = \frac{4\sigma_K^2 L_K / \bar{u}_{hub}}{(1 + 6fL_K / \bar{u}_{hub})^{5/3}} \tag{3}$$

where f is the cyclic frequency and L_k is an integral scale parameter. More information can be found in IEC 61400-1[20] or the *TurbSim User's Guide*[21].

The NREL NWTCUP model represents turbulent inflow characteristics at the NWTC, downwind of a major mountain range. A mean wind speed of 13 m/s was used. For neutral and stable flows, the NWTCUP spectra are defined by adding scaled versions of the SMOOTH-model spectra:

$$S_K(f) = \sum_{i=1}^{NumPeaks_K} p_{i,K} S_{K,SMOOTH}(F_{i,K} f) \tag{4}$$

where $NumPeaks_K$ = 2 for all wind components $K = u, v, w$ and the function $S_{K,SMOOTH}$ is defined within the SMOOTH model. More information can be found in the *TurbSim User's Guide*[21].

The sample time spacing was 0.01 seconds, corresponding to a sample rate of 100 Hz. Since the per-revolution harmonics were mainly of interest and the maximum rotor speed was 12.1 rpm, or 0.2 Hz, this sample rate was sufficient. Simulations were conducted under three conditions: (1) all three blades are healthy, (2) one of the three blades having a 5-meter shear web disbond, (3) one of the three blades having a 10-meter shear web disbond. Two hundred output variables were recorded from the simulations, including generator power, blade root moments, tri-axial blade accelerations along the span, nacelle accelerations, and many others. The first 30 seconds of simulations were discarded in analyzing the data to allow any startup transients to damp out – the *FAST User's Guide* recommends at least five seconds[13]. The total simulation time for each test, eliminating the first 30 seconds, was one hour, allowing for averaging to take place.

B. Analysis of Shear Web Disbond without Blade Sensors

In order to compare the effectiveness of shear web disbond detection methods with and without blade sensors, algorithms were first generated for determining the disbond using only the outputs from FAST that would not require blade-mounted sensors. The FAST variables which displayed significant percentage changes in their RMS value or frequency response magnitude at the operating speed given a shear web disbond were identified as key measurement channels. The rotor azimuth position output from FAST was used as the reference signal for time synchronous averaging. The rotational resampling and synchronous averaging was performed as described in Section II.

Overall, the generator power output did not change significantly between the healthy model and those models with a shear web disbond. Interestingly, a phase shift occurred in the synchronously averaged power output under the presence of a SW disbond. However, the RMS power output did not change more than ~0.035% when the three turbine models were examined under the four different wind profiles.

For all of the following discussion, axial nacelle acceleration will refer to acceleration in the x_s direction, vertical nacelle acceleration (or tower axis) will refer to acceleration in the y_s direction, and transverse (or side-to-side) nacelle acceleration will refer to acceleration in the z_s direction (see Figure 2a). For all wind cases, nacelle accelerations increased in all three directions with the presence of the shear web disbond. In addition, the percent changes were correlated with the extent of damage (i.e. length of the disbond). In addition, the x_s and y_s 1p response differences as well as the RMS differences in the z_s direction indicated the presence and severity of disbond. However, no feature could be extracted to indicate which blade contained the damage. Figure 17a shows the 1p PS magnitude percent change of nacelle acceleration in the z_s direction and Figure 17b shows the RMS percent change of nacelle acceleration in the y_s direction.

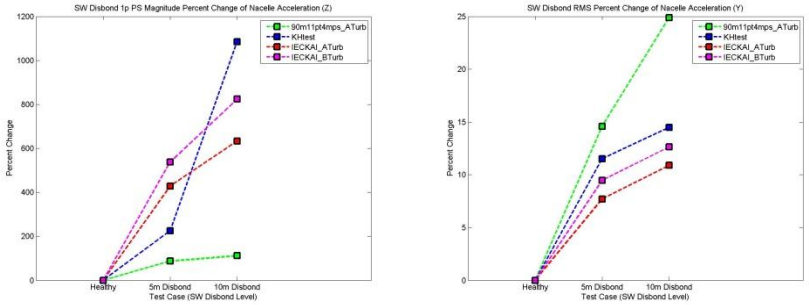

(a) **(b)**

Figure 17. (a) 1p magnitude percent change of nacelle acceleration in the z_s direction for shear web disbond; (b) RMS percent change of nacelle acceleration in the y_s direction for shear web disbond

C. Analysis of Shear Web Disbond with Blade Sensors

The blade tip acceleration response in all three directions showed positive trends as the shear web disbond was introduced and increased in length. The 1p edge-wise blade acceleration response differences are shown in Figure 18a. These 1p response differences increased significantly with increasing shear web disbond (as much as a 25% increase for a 10 meter SW disbond). The blade tip span-wise acceleration 1p response differences (shown in Figure 18b) and flap-wise acceleration RMS response differences (shown in Figure 18c) also increase in the presence and increase of a shear web disbond. Note that the 1p magnitude percent change in the side-to-side nacelle acceleration was the most sensitive parameter to a shear web disbond, but the trend lines vary for the different wind profiles. On the other hand, the blade tip acceleration responses follow very similar trends for all four wind profiles.

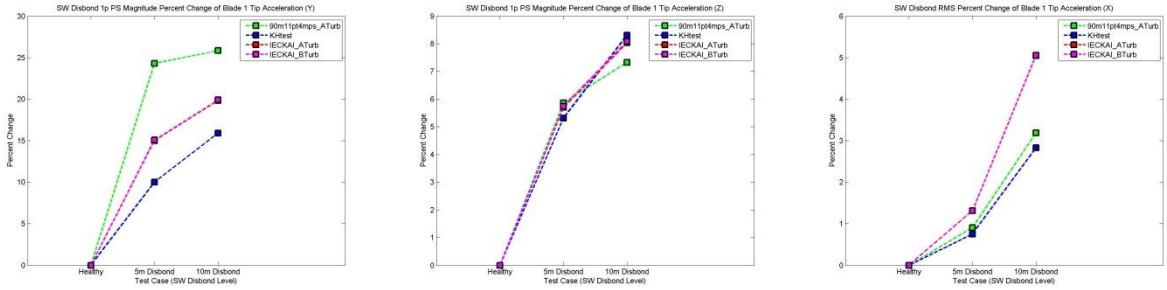

(a) **(b)** **(c)**

Figure 18. (a) 1p magnitude percent change of edge-wise blade tip acceleration for shear web disbond; (b) 1p magnitude percent change of span-wise blade tip acceleration for shear web disbond; (c) RMS response percent change of flap-wise blade tip acceleration for shear web disbond

The moment of the blade about its pitch axis at the blade root is another good indicator of a shear web disbond, as shown here. This moment can be measured using strain gages located at the root of each blade and this parameter was also shown to be a good indicator of pitch error, as shown in Section II. The blade root pitching moment 1p response differences (shown in Figure 19a) increase while the RMS response differences (shown in Figure 19b) are small and decrease with increased disbond length. The RMS response difference is very small, however the increase in the root pitching moment 1p response is expected since a shear web disbond would cause a reduction in torsional stiffness and the disbond originates at max chord, relatively close to the root of the blade. Both measurement sets also follow very similar trends for all four wind profiles as the shear web disbond is increased.

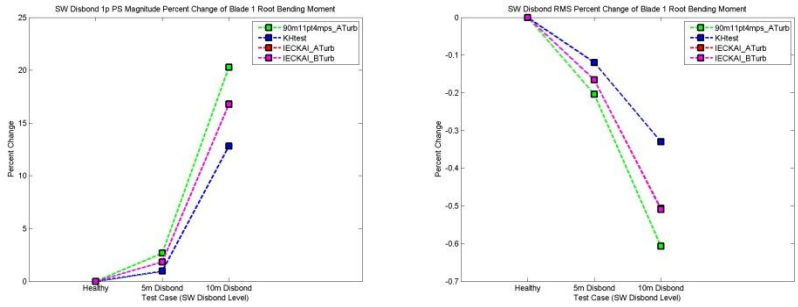

(a) **(b)**

Figure 19. (a) 1p magnitude percent change of blade root pitching moment for shear web disbond;(b) RMS response percent change of root blade pitching moment for shear web disbond

The shear web disbonds produced notable differences in the blade root acceleration response in the flap-wise direction (see Figure 20). However, it is not yet clear how sensitive this parameter would be to a disbond located further down the span of the blade. Future work involving the analysis of shear web disbonds at different locations along the blade would provide better insight.

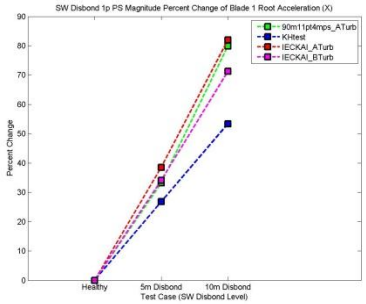

Figure 20. Blade root 1p flap-wise acceleration response differences for shear web disbond

D. Summary of Shear Web Disbond Detection Strategy

The results of these analyses can be synthesized into a flow chart, as shown in **Error! Reference source not found.** 21, for detection of shear web disbonds using a combination of sensors and analysis methods. The proposed strategy is to:

(1) Detect if a shear web disbond exists in one of the blades
(2) Determine the severity of the shear web disbond
(3) Notify turbine operator of the disbond and severity so that a repair can be scheduled or coordinated with other maintenance

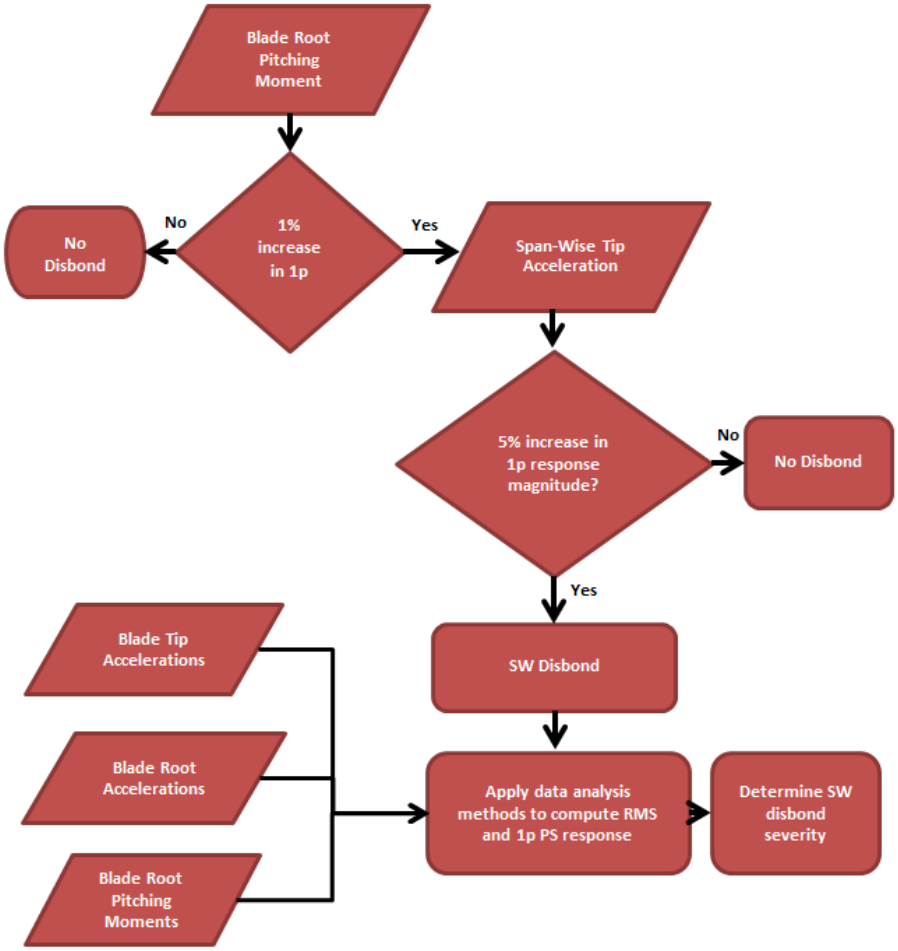

Figure 3. Shear web disbond detection flow chart

V. Conclusions

A multiscale methodology [12] has been expanded for the investigation and development of SHPM methods for offshore wind turbine blades. The method utilizes the propagation of damage from a high fidelity component level model up to a reduced order model of a full turbine so that the changes in the turbine's operational responses can be examined. Furthermore, these full turbine simulations can be used to replicate fault mechanisms such as pitch error and estimate the loads on the turbine blades which can then be propagated back to the high fidelity model to allow for further local analyses to be conducted. By investigating the effects of damage on multiple scales, the developed methodology takes advantage of available software to investigate the underlying physical consequences of damage/faults on both a local and global level which leads to the identification of operational responses that are most sensitive to these physical changes.

This document has described the application of the developed methodology to investigate the effects of rotor imbalance and a shear web disbond on an offshore 5-MW wind turbine. The 61.5 meter blade model was developed in SNL's NuMAD software and exported to ANSYS where the shear web disbond was simulated by separating the nodes of the shear web from the blade at the location of the disbond. The reduced order blade models with varying levels of damage were included into a model of an offshore turbine on a fixed monopole in 20 meters of water. The response of these offshore turbine models with varying levels of damage/imbalance was then simulated in FAST. From these simulations it was apparent that the measurements which were the most sensitive to the present and extent of the shear web disbond or pitch error were the blade tip accelerations and the root pitching moments. The aerodynamic loads from the FAST simulations were calculated and applied to the high fidelity ANSYS model which also demonstrated an increased blade tip deflection due to the presence of a shear web disbond. The structural

health of each turbine could be utilized in the optimization of damage mitigating control strategies and maintenance schedule to reduce the operations and maintenance costs associated with running an offshore wind energy plant.

Acknowledgments

We would like to acknowledge Todd Griffith, Sandia National Laboratories, as the contract monitor for this work and the U.S. Department of Energy for their continuing support of the wind energy research efforts being performed at Purdue University.

References

[1]R. Wiser and M. Bolinger, *2010 Wind Technologies Market Report*, Lawrence Berkeley
National Laboratory: Lawrence Berkeley National Laboratory. LBNL Paper LBNL-4820E, June 2011.

[2]A.C. Levitt, W. Kempton, A.P. Smith, W. Musial and J. Firestone, "Pricing offshore wind power." *Energy Policy* (In Press) 2011.

[3]B. Snyder and M.J. Kaiser, "Ecological and economic cost-benefit analysis of offshore wind energy." *Renewable Energy* 34(6), pp. 1567-1578, 2009.

[4]G. van Bussel, A.R. Henderson, C.A. Morgan, B. Smith, R. Barthelmie, K. Argyriadis, A. Arena, G. Niklasson, and E. Peltola, "State of the Art and Technology Trends for Offshore Wind Energy: Operation and Maintenance Issues," *Offshore Wind EnergyEWEA Special Topic Conference*, Brussels, Belgium, December 2001.

[5]L.W.M.M. Rademakers, H. Braam, M.B. Zaaiger, and G.J.W. van Bussel, "Assessment and optimisation of operation and maintenance of offshore wind turbines," in *Proceedings of the European Wind Energy Conference*, Madrid, Span, June 2003.

[6]Y. Amirat, M.E.H Benbouzid, B. Bensaker, and R. Wamkeue, "Condition monitoring and fault diagnosis in wind energy conversion systems: a review." In *Proceedings 2007 IEEE International Electric Machines and Drives Conference*, Vol 2., pp. 1434-1439, 2007.

[7]J. Nilsson and L. Bertling, "Maintenance management of wind power systems using condition monitoring systems – Life cycle cost analaysis for two case studies," *IEEE Transactions on Energy Conversion* 22(1), pp. 223-229, 2007.

[8]C.C. Ciang, J.R. Lee, and H.J. Bang, "Structural health monitoring for a wind turbine system: a review of damage detection methods." *Measurement Science and Technology* 19(12), pp. 1-20, 2008.

[9]F. Besnard, K. Fischer, and L. Bertling, "Reliability-centred asset maintenance – A step towards enhanced reliability availability and profitability of wind power plants" in *2010 IEEE PES Innovative Smart Grid Technologies Conference Europe (ISGT Europe)*, 2010.

[10]Z. Hameed, S.H. Ahn, and Y.M. Cho, "Practical aspects of a condition monitoring system for a wind turbine with emphasis on its design, system architecture, testing and installation," *Renewable Energy*, 35(5), pp. 879-894, May 2010.

[11]J. Jonkman, S. Butterfield, W. Musial, and G. Scott, "Definition of a 5-MW Reference Wind Turbine for Offshore System Development," NREL/TP-500-38060, Golden, CO: National Renewable Energy Laboratory, February 2009.

[12]D.T. Griffith, N. Yoder, B. Resor, J. White, and J. Paquette, , "Structural Health and Prognostics Management for Offshore Wind Turbines: An Initial Roadmap," SAND2012-10109, Sandia National Laboratories; Albuquerque, NM, Printed December 2012.

[13]J. Jonkman and L. Buhl, "FAST User's Guide," NREL/EL-500-38230, Golden, CO: National Renewable Energy Laboratory, August 2005.

[14]J. Losi, and E. Becker, "Imbalance: A danger to components," Erneuerbare Energien, August 2009.

[15]J. Giebhardt and WP7 Partners, "Condition Monitoring for Wind Turbines 'State of the Art' Report," Kassel, Germany: European Commission, 2007.

[16]M. MaCamhaoil, "Bruel & Kjaer Application Notes: Static and Dynamic Balancing of Rigid Rotors," n.d. http://www.bksv.com/doc/bo0276.pdf (accessed March 2012).

[17]Moog Incorporated, Rotor Monitoring Systems, June 2011. http://www.moog.com/literature/ICD/Moog-Wind-Rotor-Monitoring-System-Overview-en.pdf (accessed March 13, 2012).

[18]J.P. Borg and R.H. Kirchoff, "Mass and Aerodynamic Imbalance of a Horizontal Axis Wind Turbine," Journal of Solar Energy Engineering 120 (Feburary 1998): 66-74.

[19]Y. Nam, T. Yoon, K. Kim, and H. Cuong, 41. "Estimation of a Nacelle Dynamic Motion of a Wind Turbine," *Contorl, Automation, Robotics and Vision, 2008, ICARCV 2008. 10th International Conference on* , pp. 1017-1020, 2008.

[20]IEC 61400-1, "Wind turbine generator systems-Part 1: Safety requirements," 2nd edition, Geneva,
Switzerland: International Electrotechnical Commission, 1999.

[21]B.J. Jonkman and L. Kilcher, "TurbSim User's Guide: Version 1.06.00," NREL/TP-xxx-xxxx (Draft Version), Golden, CO: National Renewable Energy Laboratory, September 2012.